OPEN ACCESS



Deep Synoptic Array Science: Two Fast Radio Burst Sources in Massive Galaxy Clusters

Liam Connor¹, Vikram Ravi^{1,2}, Morgan Catha², Ge Chen¹, Jakob T. Faber¹, James W. Lamb², Gregg Hallinan^{1,2}, Charlie Harnach², Greg Hellbourg^{1,2}, Rick Hobbs², David Hodge¹, Mark Hodges², Casey Law^{1,2}, Paul Rasmussen², Jack Sayers¹, Kritti Sharma¹, Myles B. Sherman¹, Jun Shi¹, Dana Simard¹, Jean Somalwar¹, Reynier Squillace¹, Sander Weinreb¹, David P. Woody², and Nitika Yadlapalli¹, (The Deep Synoptic Array team)

¹ Cahill Center for Astronomy and Astrophysics, MC 249-17 California Institute of Technology, Pasadena, CA 91125, USA; liam.dean.connor@gmail.com

² Owens Valley Radio Observatory, California Institute of Technology, Big Pine, CA 93513, USA

**Received 2023 February 28; revised 2023 May 9; accepted 2023 May 9; published 2023 May 31

Abstract

The hot gas that constitutes the intracluster medium (ICM) has been studied at X-ray and millimeter/submillimeter wavelengths (Sunyaev–Zel'dovich effect) for decades. Fast radio bursts (FRBs) offer an additional method of directly measuring the ICM and gas surrounding clusters via observables such as dispersion measure (DM) and Faraday rotation measure. We report the discovery of two FRB sources detected with the Deep Synoptic Array whose host galaxies belong to massive galaxy clusters. In both cases, the FRBs exhibit excess extragalactic DM, some of which likely originate in the ICM of their respective clusters. FRB 20220914A resides in the galaxy cluster A2310 at z=0.1125 with a projected offset from the cluster center of $520\pm50\,\mathrm{kpc}$. The host of a second source, FRB 20220509G, is an elliptical galaxy at z=0.0894 that belongs to the galaxy cluster A2311 at the projected offset of $870\pm50\,\mathrm{kpc}$. These sources represent the first time an FRB has been localized to a galaxy cluster. We combine our FRB data with archival X-ray, Sunyaev–Zel'dovich (SZ), and optical observations of these clusters in order to infer properties of the ICM, including a measurement of gas temperature from DM and y_{SZ} of $0.8–3.9\,\mathrm{keV}$. We then compare our results to massive cluster halos from the IllustrisTNG simulation. Finally, we describe how large samples of localized FRBs from future surveys will constrain the ICM, particularly beyond the virial radius of clusters.

Unified Astronomy Thesaurus concepts: Intracluster medium (858); Radio bursts (1339); Rich galaxy clusters (2005)

1. Introduction

Galaxy clusters are massive $(10^{14}-10^{15}\,M_\odot)$, gravitationally bound objects comprised of hundreds to thousands of galaxies. Galaxies make up just a few percent of the total cluster mass. The dominant component of baryons by mass and volume is in the hot intracluster medium (ICM) made of diffuse gas with $n_e \approx 10^{-3}~{\rm cm}^{-3}$ and $T_e \approx 10^7-10^8~{\rm K}$. Within a sufficiently large volume (e.g., the virial radius), the ratio of dark matter to baryons approximately matches the universal value (Eckert et al. 2019), which is not true for smaller halos where feedback is expected to expel gas beyond the virialized dark matter halos (Tumlinson et al. 2017).

The ICM has been studied in great detail at X-ray wavelengths for the past 50 yr (Sarazin 1986). Thermal bremsstrahlung emission from gas heated to 2–15 keV is observed out to the virial radii of clusters (1–2 Mpc), tracing the radial distribution of the ICM gas (Ghirardini et al. 2019). The ICM reaches such high temperatures by adiabatic compression and shock heating as the gas reaches hydrostatic equilibrium within the potential well (Voit 2005). Free–free emission scales with emissivity and the specific X-ray luminosity can be written as an integral of plasma density

Original content from this work may be used under the terms of the Creative Commons Attribution 4.0 licence. Any further distribution of this work must maintain attribution to the author(s) and the title of the work, journal citation and DOI.

squared,

$$L_X \approx \int n_e^2 \Lambda(T_e) dV,$$
 (1)

where n_e is the number density of free electrons and $\Lambda(T_e)$ characterizes the temperature dependence of the X-ray emission. The total mass can then be inferred from the cluster's X-ray luminosity (Pratt et al. 2009). X-ray spectroscopy can also be used to measure the gas temperature (Böhringer & Werner 2010) and its velocity structure (Hitomi Collaboration et al. 2016).

The hot plasma in the ICM is also observable at millimeter/submillimeter wavelengths through the thermal Sunyaev–Zel'dovich (SZ) effect, whereby photons in the cosmic microwave background (CMB) are inverse Compton scattered by thermal electrons (Mroczkowski et al. 2019). This leads to spectral distortions in the CMB at the level of 10^{-4} – 10^{-5} . SZ observations of the ICM are parameterized by the Compton Y parameter, which is given by the integral of electron thermal pressure along the line of sight,

$$y_{\rm SZ} = \frac{k_B \sigma_T}{m_e c^2} \int n_e T_e dl, \qquad (2)$$

where k_B is Boltzmann's constant, σ_T is the Thomson cross section, m_e is electron mass, and c is the speed of light.

Fast radio bursts (FRBs) offer an additional probe of the ICM of massive galaxy clusters. FRBs are short-duration $(10^{-2}-10^2 \text{ ms})$ radio transients that have been detected over

cosmological distances ($z\lesssim1.5$; Cordes & Chatterjee 2019; Petroff et al. 2019). To date, $\mathcal{O}(10^3)$ sources have been discovered (Petroff et al. 2016; CHIME/FRB Collaboration et al. 2021), but only two dozen have been localized with sufficient angular precision to identify a host galaxy (Chatterjee et al. 2017; Ravi et al. 2019; Bhandari et al. 2020; Heintz et al. 2020). Propagation effects imparted on the radio pulse encode information about the plasma through which the burst traveled. Dispersion measure (DM) is an integral of line-of-sight electron density and is given by

$$DM = \int n_e \, dl. \tag{3}$$

Unlike with thermal X-ray emission or SZ observations of the ICM, the FRB DM is detectably impacted by *all* plasma between us and the source, not just 10^{6-8} K gas. This is both a blessing and a curse: FRB DMs will probe plasma in the host galaxy, the circumgalactic medium (CGM), the ICM of intervening or host clusters, the intergalactic medium (IGM), and the Milky Way's interstellar medium (ISM). For individual FRB sight lines, these terms must be explicitly modeled. An FRB that is impacted by a galaxy cluster will have the following "DM budget,"

$$DM_{obs} = DM_{MW} + DM_{IGM} + \frac{DM_{ICM}}{1 + z_c} + \frac{DM_{host}}{1 + z_{frb}},$$
 (4)

where z_c and z_{frb} are the cluster and FRB redshifts, respectively. Here, DM_{host} is the host galaxy contribution. The observed DM is likely dominated by the IGM for most FRBs. Still, it is important to be specific about what is meant by the IGM. In Macquart et al. (2020), the relationship between DM_{cosmic} and source redshift includes all extragalactic gas between the Milky Way and the host galaxy. DM_{cosmic} therefore includes the CGM, intragroup medium, ICM, and IGM. All of those terms correlate with source distance because the optical depth of halos increases with redshift. In this work, we take the IGM to be ionized gas that resides outside of virialized dark matter halos (McQuinn 2016).

For sources that intersect or are embedded in galaxy clusters, the largest DM contribution may be from the ICM (Prochaska & Zheng 2019). For example, a cluster with $\langle n_e \rangle = 10^{-3} \text{ cm}^{-3}$ and $R_{200} = 1$ Mpc will lead to $\mathrm{DM_{ICM}} \sim 10^3$ pc cm⁻³ for low-impact parameters. This value is more than double the typical contribution from the IGM for a source at z=0.5% and 70% larger than the mean $\mathrm{DM_{obs}}$ of CHIME/FRB sources (Macquart et al. 2020; CHIME/FRB Collaboration et al. 2021). The polarization properties of FRBs can help measure the magnetic field of the ICM. Faraday rotation measure (RM) is an integral of the free electrons, weighted by the line-of-sight magnetic field strength,

$$RM = \frac{e^3}{2\pi m_e^2 c^4} \int B_{\parallel} n_e(l) dl,$$
 (5)

where *e* is the charge of an electron. While other radio objects can provide cluster RMs (van Weeren et al. 2019), FRBs are unique among extragalactic sources in their ability to measure both RM and DM. Therefore, if one can isolate the components of RM and DM that are due to the ICM, the mean line-of-sight magnetic field strength in the cluster can be determined by their

ratio,

$$\langle B_{\parallel,\text{ICM}} \rangle = 1.23 \ \mu\text{G} \frac{\text{RM}_{\text{ICM}}}{\text{DM}_{\text{ICM}}},$$
 (6)

where RM and DM are given in the standard units of rad m⁻² and pc cm⁻³, respectively. The application of FRBs to the ICM has been considered in previous works, including the detection of an FRB in the direction of the Virgo cluster by ASKAP (Agarwal et al. 2019). In that case, the localization precision was insufficient to determine a host galaxy, so it was unclear if the source was embedded in, or behind, the cluster. Another unlocalized source, FRB 20190116A (CHIME/FRB Collaboration et al. 2019) is likely within ~ 5 Mpc of the Coma cluster in projection and may be dispersed by filamentary structure extending from the cluster (Hallinan et al. 2019a). Fujita et al. (2017) investigated the application of FRBs to the warm-hot intergalactic medium (WHIM) at the outskirts of galaxy clusters, where X-ray observations are difficult due to the n_e^2 dependence of emissivity. Nonetheless, most of the effort in studying halo gas with FRBs has been devoted to the CGM (Prochaska & Zheng 2019; Ravi 2019; Lee et al. 2022). That is because the CGM is more difficult to detect than the ICM using traditional means (X-ray and SZ observations are much less sensitive to the gas in galaxy-scale halos) and because of the CGM's significance in galaxy formation and feedback processes. Connor & Ravi (2022) presented the first statistical evidence for the impact of halo gas on FRBs and demonstrated the importance of considering galaxy groups on FRB DM budgets. Raf (2021) saw evidence in the CHIME/ FRB sample for a population of FRBs with significant local excess DM, which they found could plausibly arise from galaxies within cluster-mass halos. As we demonstrate, current and future FRB surveys will find a significant number of sources that are impacted by galaxy clusters, and understanding their effects and prevalence are important for CGM studies, in addition to studying the ICM itself.

In this work we make the first unambiguous detection of FRB sources that belong to a galaxy cluster. Both sources were discovered by the real-time FRB survey on the Deep Synoptic Array (DSA-110).³ The DSA-110 is a radio interferometer at the Owens Valley Radio Observatory (OVRO) that was built to localize FRBs with ~arcsecond precision. A detailed account of the instrument will be presented in V. Ravi et al. (2023, in preparation). During the observations presented in this work, the DSA-110 was operating in its commissioning phase with 63 antennas collecting data, as described in Ravi et al. (2023a).

In Section 2 we describe the radio properties of two FRBs using the DSA-110. We describe the two massive clusters of which the FRB host galaxies are members. A companion paper details the interferometric localizations of FRB 20220509G and FRB 20220914A as well as their unusual host galaxies (Sharma et al. 2023). In Section 3.2 we model the DM contribution from the ICM for both sources, combining our radio data with archival X-ray, SZ, and optical data to infer properties about the clusters' respective ICM. Finally, we compare our results with clusters found in the IllustrisTNG simulation.

³ https://deepsynoptic.org

Table 1

The Radio Properties of Two Galaxy Cluster FRBs

| Source | R.A. (deg) | Decl. (deg) | Z_{gal} | $\mathrm{DM}_{\mathrm{obs}}$ | $\mathrm{DM}_{\mathrm{MW}}$ | RM_{obs} | τ (ms) | F (Jy ms) | b_{\perp} (kpc) |
|---------------|---------------|----------------|-----------|------------------------------|-----------------------------|------------|----------------------------|--------------|-------------------|
| FRB 20220914A | 282.0568 | 73.3369 | 0.1139 | 631.29 | 47/55 | N/A | $< 0.080 \\ 0.08 \pm 0.02$ | 2.2 | 520 ± 50 |
| FRB 20220509G | 282.6700 | 70.2438 | 0.0894 | 269.53 | 46/55 | -110(1) | | 5.5 | 870 ± 50 |

Note. DM and RM are reported in pc cm⁻³ and rad m⁻², respectively. The scattering timescale, τ , is referenced to 1.4 GHz. The two Galactic ISM DM estimates listed are YMW16 and NE2001. R.A. and decl. are in epoch J2000.

 Table 2

 The Properties of Two Galaxy Clusters that Host the FRBs Presented in This Paper

| Cluster | R.A. (deg) | Decl. (deg) | Richness | $z_{ m clust}$ | $M_{500} \ (M_{\odot})$ | R ₅₀₀ (kpc) | $L_{\rm X}$ (erg s ⁻¹) | Y _{5R500} (arcmin ²) |
|----------------|----------------------|-------------------|------------|---------------------|--|------------------------|---|---|
| A2310 A2311 | 281.81708 282.497 | 73.3472 70.376 | 124 190 | 0.1125 0.0899(1) | 1.7×10^{14} 1.6×10^{14} | 810 800 | 8.3×10^{43} 4.7×10^{43} | $0.85 \pm 0.35 \times 10^{-3}$ $0.81 \pm 0.36 \times 10^{-3}$ |

Note. L_X is the X-ray luminosity at 0.1–2.4 keV within R_{500} .

2. Cluster FRBs

FRB 20220914A The radio properties of FRB 20220509G are listed in Table 1. The observed parameters of their respective host galaxy clusters are given in Table 2. The two FRBs presented here are from distinct galaxy clusters but are relatively nearby on the sky-separated by just 3.1 degrees. DSA-110 is a transit instrument that was parked at decl. $\sim +70$ for most of the 2022 commissioning period. For this reason, most of our initial sample of sources falls on a ring in R.A., and several pairs are within a few degrees of each other. Below we described observations of the FRBs and their host galaxies, as well as archival data obtained for the galaxy clusters.

2.1. FRB 20220914A

FRB 20220914A was detected at MJD 59,836.1459660. Follow-up analysis found an optimal DM of 631.3 pc cm⁻³ and a pulse FWHM of 140 μ s. With a signal-to-noise ratio (S/N) of 13.4 and system-equivalent flux density of 140 Jy, the fluence of the burst was roughly 2.2 Jy ms. The pulse is shown in Figure 1. Offline interferometric localization found the position of the FRB to be R.A. J2000, decl. J2000 = 18^h48^m13^s.63, $+73^{d}20^{m}12^{s}89$, the centroid of which is 1.16 from a galaxy with spectroscopic redshift z=0.1139. The expected DM from the Milky Way at these Galactic coordinates is roughly 50 pc cm⁻³ from NE2001 (Cordes & Lazio 2002) and 47 pc cm⁻³ from YMW16 (Yao et al. 2017). The IGM is expected to contribute 50–120 pc cm⁻³ at this redshift, suggesting that FRB 20220914A has significant extragalactic DM excess.

We find no evidence of scattering, placing an upper limit of τ < 80 μs at 1.4 GHz. Polarimetric analysis found no detectable polarization, and no RM was determined after searching a range of -10^6 to $+10^6$ rad m⁻². The upper limits on the polarization fraction were L/I < 15% and V/I < 20%.

2.1.1. ABELL 2310 Galaxy Cluster

The position of FRB 20220914A was crossmatched with both the DESI Legacy Imaging Surveys Data Release 8 (DR8) galaxy catalog (Dey et al. 2019) and a DR8 cluster/group catalog that was independently assembled using

photometric redshifts in the Legacy Imaging Surveys and spectroscopic redshifts, when available. (Yang et al. 2021). We find that the host galaxy of FRB 20220914A is a member of the massive galaxy cluster A2310 (Abell 1958). The overdensity in this direction can be seen in Figure 2. According to the DESI Legacy Imaging Survey DR8 group/ cluster catalog (Yang et al. 2021), this cluster has richness 124 (i.e., number of member galaxies), $M_{180} = 2.5 \times 10^{14}$ M_{\odot} , with a brightest cluster galaxy (BCG) at spectroscopic redshift z = 0.1125. The cluster is also in the Meta-Catalog of X-Ray Detected Clusters of Galaxies (MCXC) with source name J1847.2+7320 (Piffaretti et al. 2011). The X-ray surface brightness centroid is at 18h47m16.s 73d20m50s (Piffaretti et al. 2011). The FRB offset from this position is 4.22′, suggesting a projected physical impact parameter of 520 kpc. The X-ray luminosity within R_{500} is $8.31 \times 10^{43} \text{ erg s}^{-1}$, which gives $M_{500} = 1.69 \times 10^{14} M_{\odot}$ using an empirical $L_X - M$ relation (Pratt et al. 2009; Piffaretti et al. 2011).

The cluster has also been detected via the thermal SZ effect and is listed in the Planck SZ2 cluster catalog as PSZ2 G104.29 +26.17 (Planck Collaboration et al. 2016a). The SZ-derived mass based on a hydrostatic mass calibration is $M_{500}=1.94\pm0.28\times10^{14}\,M_{\odot}$ (Planck Collaboration et al. 2014), and its SZ centroid has a physical offset from FRB 20220914A of \sim 380 kpc. We have also analyzed the Planck MILCA y map from Planck Collaboration et al. (2016b) using the techniques described in Sayers et al. (2016) to obtain both a two-dimensional projected model of the cluster $y(\theta)$, along with the total integrated SZ signal Y_{5R500} . In brief, we assume the cluster follows the profile shape given by Arnaud et al. (2010), with the scale radius set by the X-ray value of R_{500} and centered on the X-ray centroid. We then determine the best-fit normalization of this model, with the uncertainty on this normalization estimated from fits to 100 random realizations of the Planck noise. The result is $Y_{5R500} = 0.85 \pm 0.35$ arcmin².

The point-spread function (PSF) of Planck is large, so we take the offset between FRB 20220914A and A2310 to be the separation between the X-ray centroid and the FRB's host galaxy. This gives a projected physical offset of 520 ± 50 kpc. In Figure 3 we show the filtered X-ray data with a contour for the SZ emission region, as well as a zoomed-in image on the

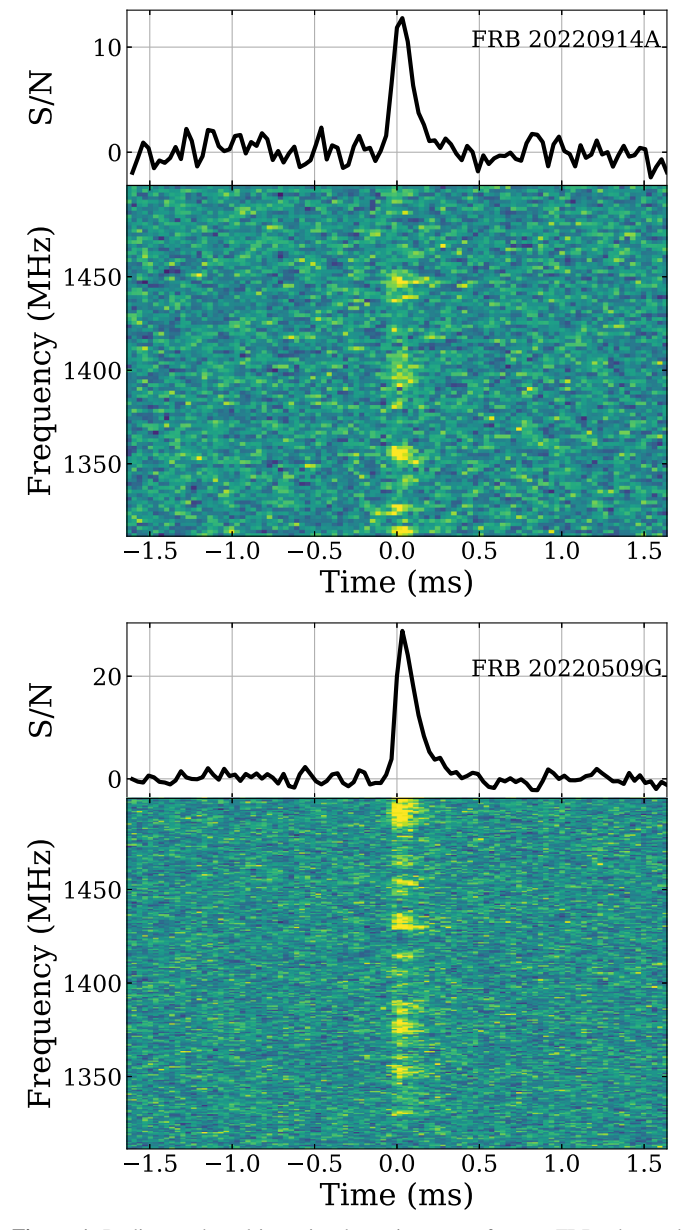


Figure 1. Dedispersed total-intensity dynamic spectra for two FRBs detected by DSA-110. Both FRBs reside in galaxies that belong to massive galaxy clusters.

optical host galaxy image. The X-ray intensity data is taken from the public archive of X-ray clusters⁴ (Xu et al. 2022).

The relative redshift between the host galaxy of FRB 20220914A and the BCG is $\Delta z = +0.0014$, indicating the host has a recession velocity of roughly 420 km s⁻¹. We do not know the radial position of the FRB within the cluster, but we have good reason to believe it is not near the front. We take the radial position to be $l_{\rm LOS}$, which is zero at the distance of the cluster center and negative behind the cluster. The radial distribution of galaxies in clusters is well described by a Navarro–Frenk–White profile with concentration parameter c=2.6 (Budzynski et al. 2012). With a virial radius of 800 kpc, the probability distribution of the galaxy radius peaks around 300 kpc and declines toward larger radii. Therefore, for an impact parameter beyond 300 kpc, the most likely $l_{\rm LOS}$ is zero.

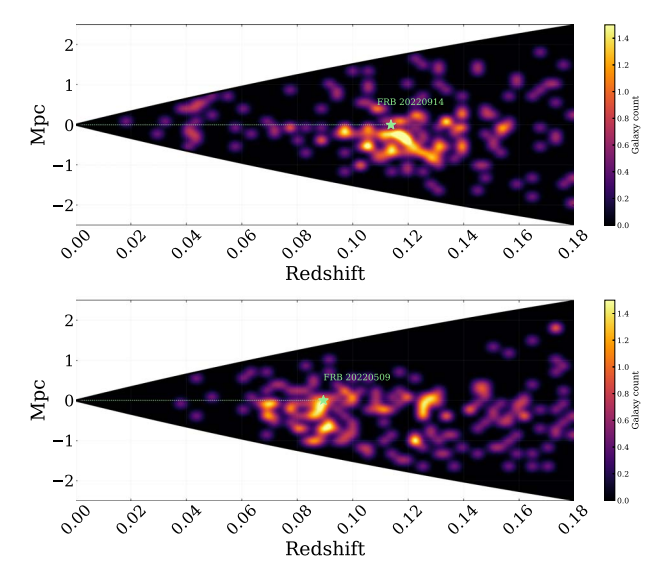


Figure 2. Slice plots of the smoothed galaxy number density within 5' of each FRB line of sight. The galaxy data are from the DESI Legacy Imaging Survey DR8 and are mostly photometric redshifts.

More convincingly, as we show in Section 3.2, the FRB has significant excess dispersion that likely comes from the ICM. The magnitude of this extra DM cannot easily be explained by the IGM or the host galaxy, so $l_{\rm LOS}$ is likely smaller than several hundred kpc.

2.1.2. The Host Galaxy of FRB 20220914A

The FRB 20220914 has been localized to a typical late-type spiral galaxy at R.A. (J2000) = 18:48:13.9580 and decl. (J2000) = +73:20:10.703 (Sharma et al. 2023). The spectroscopic redshift of the galaxy, as measured from optical spectra acquired with Keck I/LRIS, is 0.1139 ± 0.0001 . A detailed spectral energy distribution analysis revealed a stellar mass of $\log M_*(M_\odot) = 9.99^{+0.09}_{-0.09}$. The constrained star formation history indicates significant recent star formation with several starbursts over the last 3.5 Gyr, thus reflecting a wide probability distribution for the age of its progenitor.

2.2. FRB 20220509G

The FRB source FRB 20220509G had an arrival time of MJD 59,708.4944991 at reference frequency of 1500 MHz. Its optimal DM was 269.53 pc cm⁻³ and had a fluence of 5.5 Jy ms. Its dedispersed dynamic spectrum is shown in Figure 1. Offline interferometric localization found that the source is at R.A. J2000, decl. J2000 = $18^h50^m40^s8$, +70d14m37.8, with a 90% error ellipse with axes 4".7 and 3".2 in R.A. and decl. This is within 6" of a massive galaxy with spectroscopic redshift z = 0.0894. The Galactic ISM DM estimates are 55 pc cm⁻³ from NE2001 and 46 pc cm⁻³ from YMW16. The expected IGM contribution at this redshift is roughly 75 pc cm⁻³ but with significant uncertainty. We analyze the source's DM budget in Section 3.2.

The burst was fit with a scattering tail plus a Gaussian component. We find evidence of scattering with a timescale of $80\pm20~\mu s$ at $1.4~\rm GHz$ and a Gaussian component that is $30\pm10~\mu s$. Offline polarimetric analysis found that FRB 20220509G was nearly 100% linearly polarized with an RM of $-111.5\pm1.5~\rm rad~m^{-3}$ in the observer frame. This is significantly larger than the Galactic RM foreground value of

⁴ https://github.com/wwxu/rxgcc.github.io

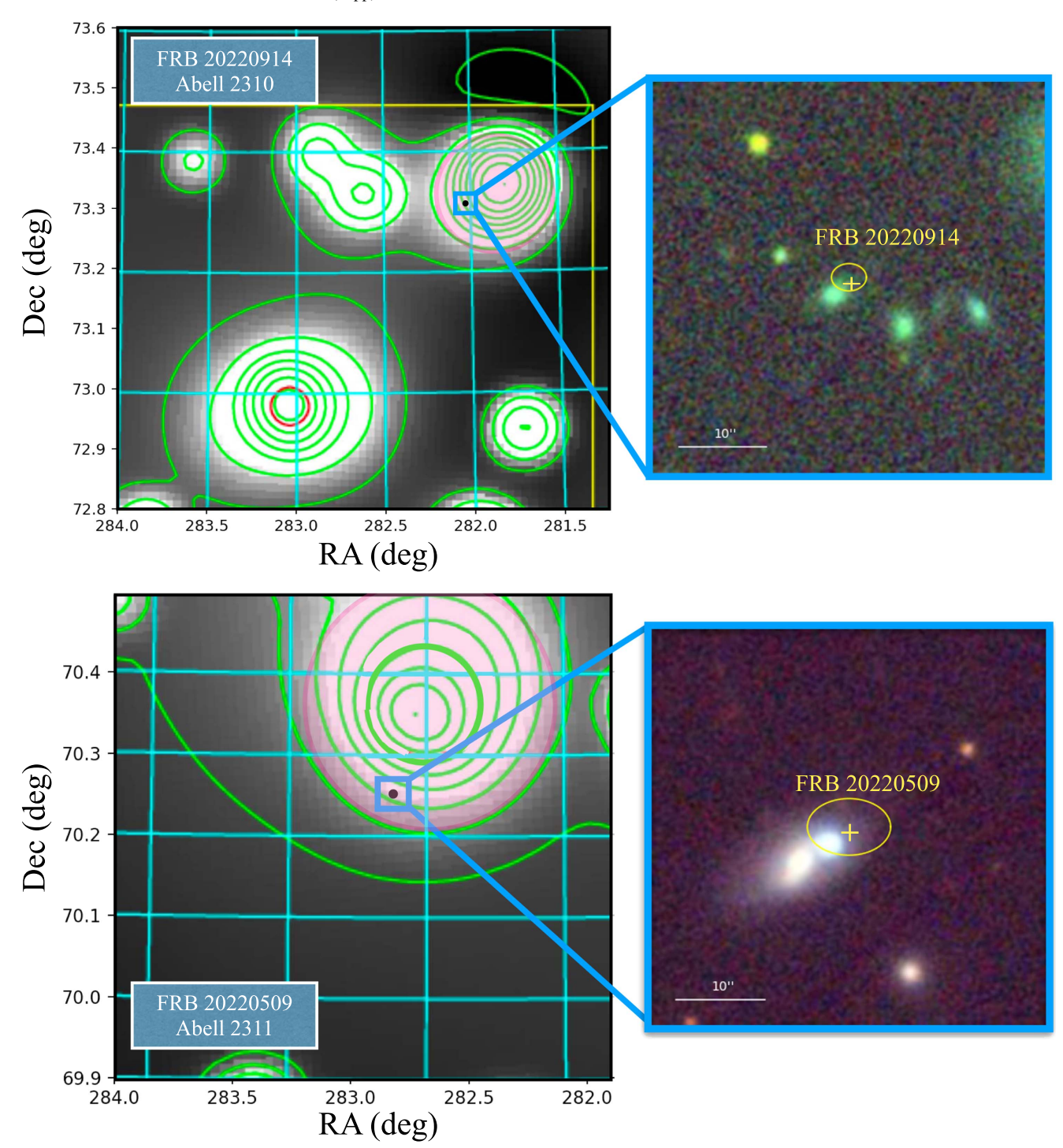


Figure 3. The two FRB sources reported in this work with their respective host galaxies and galaxy clusters. The left column images show filtered ROSAT X-ray intensity (Xu et al. 2022) for galaxy cluster A2310 (top) and A2311 (bottom). The magenta circle in the top left panel has a radius of 1 Mpc and denotes the location of the SZ cluster from the PSZ2 catalog. The bottom panel magenta circle corresponds to our SZ measurement for A2311. The right columns show insets on the position of FRB 20220914A (top) and FRB 20220509G (bottom) plotted over a PanSTARRS1 riz-band image (Chambers et al. 2016, PanSTARRS1).

 $-9\pm16~{\rm rad~m}^{-3}$. The burst's position angle (PA) is flat across the pulse. The polarization properties of FRB 20220509G are shown in Figure 4.

2.2.1. A2311 Galaxy Cluster

The host galaxy of FRB 20220509G is a member of the galaxy cluster A2311 (Abell 1958). According to the DESI Legacy Imaging Survey DR8 cluster/group catalog (Yang et al. 2021), the cluster's richness is 190 with $M_{180} = 2.5 \times 10^{14} \, M_{\odot}$,

determined by the velocity dispersion of member galaxies. The radius at which the average enclosed density is 500 times the critical density is $R_{500} = 800$ kpc. The X-ray luminosity within R_{500} is $L_X = 4.7 \times 10^{43}$ erg s⁻¹ with an inferred mass of $M_{500} = 1.6 \times 10^{14} M_{\odot}$. The cluster does not have a published SZ detection and is not in the Planck SZ2 cluster catalog. However, we have analyzed the Planck MILCA y map for this cluster in the same way as for A2311, finding $Y_{5R500} = 0.81 \pm 0.36 \times 10^{-3}$ arcmin².

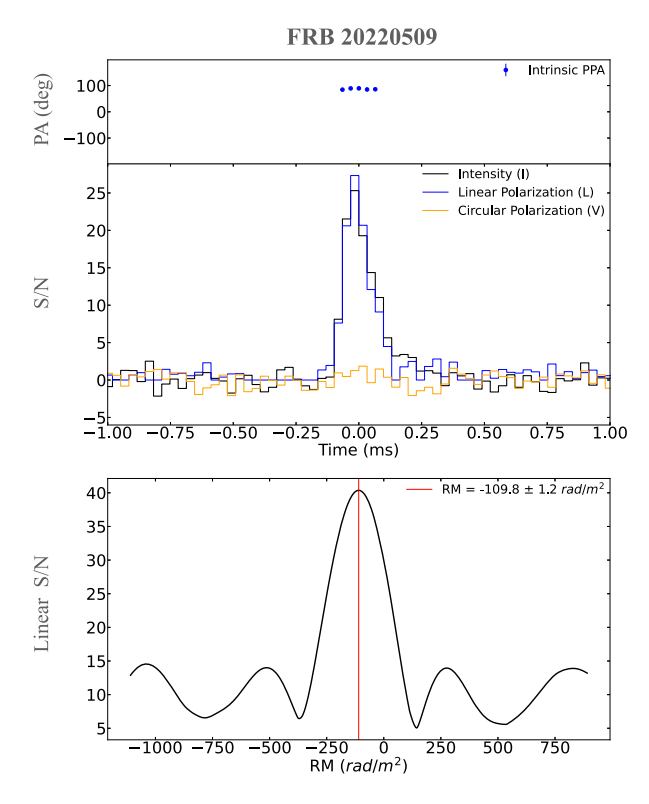


Figure 4. The polarization properties of FRB 20220509G. The top panel shows a flat PA across the pulse, and the middle panel shows the linearly polarized pulse profile. The bottom panel is the Faraday spectrum with a peak at $RM = -111.5 \text{ rad m}^{-2}$.

The filtered ROSAT X-ray intensity is shown in Figure 3. The projected physical offset between FRB 20220509G and the X-ray centroid is 870 ± 50 kpc, placing the FRB at a minimum radius of just beyond R_{500} .

2.2.2. The Host Galaxy of FRB 20220509G

The likely host galaxy of FRB 20220509 is an early-type elliptical galaxy with insignificant ongoing star formation and hence stands out as a quiescent galaxy in the known population of FRB hosts (Sharma et al. 2023). The measured spectroscopic redshift of the host is 0.0894 ± 0.0001 , and a detailed spectral energy distribution analysis reveals a stellar mass of $\log M_*(M_\odot) = 11.13^{+0.02}_{-0.02}$ with star formation rate averaged over the last $100 \, \text{Myr}$ of $0.08^{+0.06}_{-0.04}$. An old stellar population implies a long delay between the time of occurrence of this FRB and the formation of its progenitor, thus opening another window of progenitors with long delay times.

3. Data Analysis

We now seek to synthesize the FRB radio properties with observations of their host galaxies and host clusters. This will allow us to infer the impact of the ICM on FRB 20220509G and FRB 20220914A. Neither host galaxy has a high rate of star formation. The early-type host of FRB 20220509G, in particular, is not expected to have a significant ISM that would contribute to local dispersion (Lees 1992). In this section, we estimate the origin of scattering, DM, and RM and model the contribution of the ICM to each propagation effect.

3.1. Scattering and Scintillation

Both FRB sources show evidence of scintillation that is consistent with a nearby scattering screen in the Milky Way. FRB 20220509G and FRB 20220914A have decorrelation bandwidths of $\Delta \nu = 3.1 \pm 0.7 \, \text{MHz}$ and $\Delta \nu = 2.51 \pm 0.7 \, \text{MHz}$ 0.16 MHz, respectively. Since the two sources are only separated by a few degrees, it is unsurprising that their decorrelation bandwidth and modulation indexes are similar. However, the presence of fully modulated scintillation is physically interesting in the case of FRB 20220509G, which also shows evidence of temporal scattering. The presence of both scattering and spectral scintillation allows one to place constraints on the geometry of the two scattering screens. Scattering causes angular broadening, and if that broadening were too large, the FRB would be resolved out by the scattering screen in our Galaxy (Masui et al. 2015; Connor et al. 2016; Simard & Ravi 2021).

For a given scattering timescale, angular broadening is maximal when the screen is halfway between us and the source. Therefore, if the screen were in the CGM of an intervening galaxy at $z \sim 0.05$, we would not expect FRB 20220509G to scintillate. Following Equation (48) in Simard & Ravi (2021), we place an upper limit on the distance between the FRB source and the first scattering screen to be ≤ 140 kpc. This leads to three scenarios for the origin of the temporal scattering in FRB 20220509G, each of which is plausible but somewhat surprising given the early-type host galaxy and the hot, smooth ICM in which it is embedded. The scattering could be in the ISM of the host galaxy at \sim kpc scales from the FRB emitting source. This would require an unusual sight line given the lack of $H\alpha$ emission and limited turbulence in the ISM of elliptical galaxies (Seta et al. 2021; Ocker et al. 2022). Alternatively, it could arise in the immediate vicinity of the source, such as in a stellar wind, analogous to the scattering in FRB 20190520 (Anna-Thomas et al. 2023; Beniamini et al. 2022; Niu et al. 2022; Ocker et al. 2023). A third option is that it could be near the host galaxy in the ICM, perhaps in the outflows or CGM of the host.

3.2. DM from the ICM

We model the DM along the line of sight to each FRB in order to generate a probability distribution for the ICM contribution. The probability density function (PDF, denoted here by \mathcal{P}) of a sum of independent variables is the convolution of their individual PDFs. The DM terms are not strictly independent, but we find that the convolution relation for a sum of variables is a good approximation in this case. Using Equation (4), we find

$$\mathcal{P}(DM_{ICM}) = \mathcal{P}(DM_{obs})^* \mathcal{P}(-DM_{MW}) \times {}^*\mathcal{P}(-DM_{IGM})^* \mathcal{P}(-DM_{host}),$$
(7)

where $\mathcal{P}(\mathrm{DM}_{\mathrm{obs}})$ is Gaussian with variance determined by the measurement error on the observed DM. Here the DMs are all in the observer frame, so we must multiply by $1+z_c$ when estimating the DM from the ICM. We assert that the probability density must be zero for negative DM.

For FRB 20220914A, we place an upper limit on DM_{host} to be 50 pc cm⁻³ based on the strong upper limit on temporal scattering. We take $\mathcal{P}(DM_{host})$ to be a uniform distribution between 0 and 50 pc cm⁻³ because we do not have a strong motivation for a preferred DM peak in the distribution.

Previous detections of unscattered FRBs do not have a robust measurement of local DM on which to base an empirical distribution. There is reason to believe the local DM contribution is very small for other similar FRB sources. For example, FRB 20180916B (Pastor-Marazuela et al. 2021) and FRB 20220319D (Ravi et al. 2023a) have comparable upper limits on local scattering and likely have DM $_h \leqslant 20~\rm pc~cm^{-3}$. The local (<150 kpc) contribution to the DM of FRB 20220509G is less certain due to the presence of both scattering and scintillation. We assume a flat prior between 0 and 100 pc cm $^{-3}$.

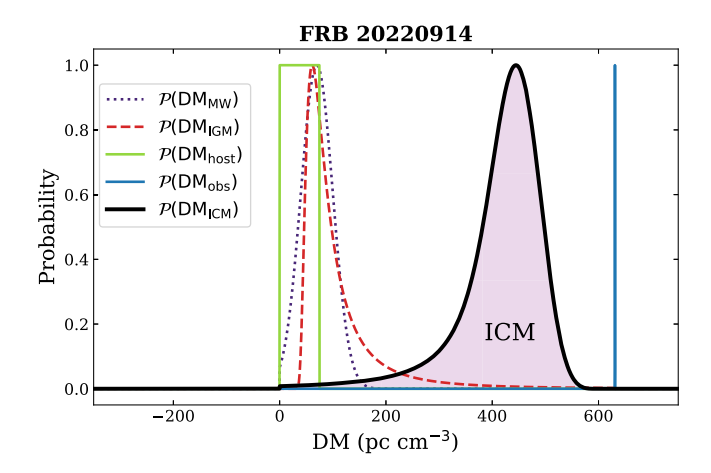
For $\mathcal{P}(\mathrm{DM_{IGM}})$, we use the IllustrisTNG simulation to estimate the distribution of DM from the IGM for a source at a few hundred Mpc along similar sight lines to our FRBs. We take the functional form of DM_{IGM} found by Zhang et al. (2021) for FRBs at $z\approx 0.1$, who also used IllustrisTNG. However, we independently estimate the mean DM_{IGM} for sight lines that intersect massive halos with $M_{500}>10^{13.5}\,M_{\odot}$. We then exclude DM contribution from the halo itself to estimate the mean of DM_{IGM} for that subset of sightlines. By doing this we account for correlations in the universe's matter distribution: sight lines that intersect clusters are more likely to intersect filaments and less likely to pass through voids, compared to typical positions. We find that for $z\lesssim 0.1$,

$$\langle \mathrm{DM}_{\mathrm{IGM}} \rangle \approx 25 \ \mathrm{pc} \ \mathrm{cm}^{-3} \left(\frac{\mathrm{D}_{A}}{100 \ \mathrm{Mpc}} \right),$$
 (8)

where D_A is the angular diameter distance. This gives a mean value of $107 \, \mathrm{pc \, cm^{-3}}$ with a 90% confidence interval on $\mathrm{DM_{IGM}} = 55\text{--}300 \, \mathrm{pc \, cm^{-3}}$ for FRB 20220914A. For FRB 20220509G we find a mean value of 76 pc cm⁻³ with a 90% confidence interval on $\mathrm{DM_{IGM}} = 45\text{--}204 \, \mathrm{pc \, cm^{-3}}$. The estimated IGM DM distributions are shown in Figure 5 as dashed red curves.

In these FRB directions, the Milky Way contribution is taken to be normally distributed with mean $70\,\mathrm{pc\,cm^{-3}}$ and standard deviation $30\,\mathrm{pc\,cm^{-3}}$. This value includes the Galactic halo. These values are based on NE2001 (Cordes & Lazio 2002) and YMW16 (Yao et al. 2017) and recent evidence that the Milky Way halo contribution to DM is smaller than previously thought (Bhardwaj et al. 2021; Cook et al. 2023; Ravi et al. 2023b). The two FRB sources are nearby on the sky, allowing us to use similar estimates for $\mathcal{P}(DM_{MW})$.

We have attempted to make conservative estimates on the uncertainty of each component of the observed DM, which will result in a wider inferred DM_{ICM} distribution. We warn that the various elements in the DM budget were estimated by different means and are subject to modeling uncertainties. With these caveats, the resulting probability distribution of the ICM contribution to the DM is shown in Figure 5. We find that A2310's ICM adds 265-511 pc cm⁻³ at 90% confidence to the observed DM of FRB 20220914A. In the frame of the cluster, this range is $295-568 \,\mathrm{pc} \,\mathrm{cm}^{-3}$. These values make it unlikely that the host galaxy is near the front of the cluster as such a high DM_{ICM} requires a significant path through the intracluster medium. In the case of A2311, we find a 90% confidence interval of 16– $172\,\mathrm{pc}\;\mathrm{cm}^{-3}$ for $\mathrm{DM}_{\mathrm{ICM}}$ in the cluster frame. This range is consistent with an FRB embedded in a $1.6 \times 10^{14} M_{\odot}$ cluster at a projected offset of ~870 kpc. Still, it is difficult to say with certainty that the FRB's majority DM



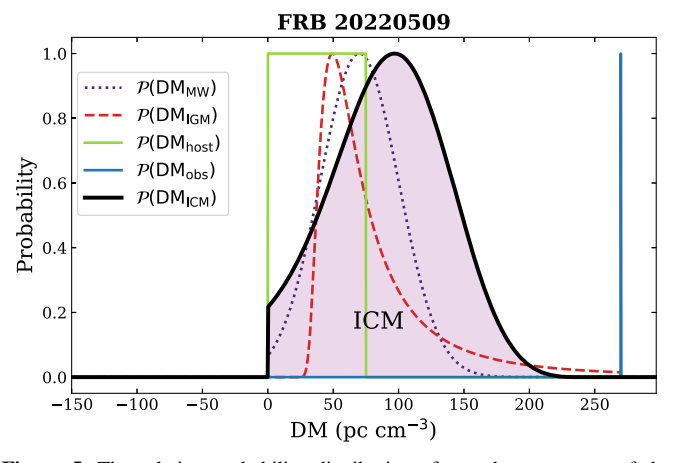


Figure 5. The relative probability distributions for each component of the observed FRB DMs. The distributions of DM_{ICM} are shown in the purple shaded region under the black curves.

component is the ICM due to the presence of scattering and larger projected impact parameter of the host.

3.3. ICM Magnetic Field

FRBs are the only known cosmological sources for which both DM and RM can be measured. If DM_{ICM} and RM_{ICM} can be determined, FRBs allow us to measure the mean line-of-sight magnetic field strength of a galaxy cluster, as shown in Equation (6). The observed RM of FRB 20220509G is -111.5 ± 1 rad m $^{-2}$, compared with the expected Milky Way foreground RM of $-9\pm16\,\mathrm{rad}\,\mathrm{m}^{-2}$ in that direction (Hutschenreuter et al. 2022). If the extragalactic RM is dominated by the ICM, then the cluster-frame RM is $\approx 120\,\mathrm{rad}\,\mathrm{m}^{-2}$, and we can use $\mathcal{P}(\mathrm{DM_{ICM}})$ to infer $\langle B_{\parallel,\mathrm{ICM}}\rangle$ at the impact parameter of FRB 20220509G. We find that the average magnetic field strength is 0.7–7.5 $\mu\mathrm{G}$. Again, this is subject to the assumption that the observed RM is dominated by the ICM.

The values we obtain for both RM and $\langle B_{\parallel,\rm ICM} \rangle$ are in line with previous observations, as well as magnetohydrodynamical (MHD) simulations of galaxy clusters (Carilli & Taylor 2002; Marinacci et al. 2018). Böhringer et al. (2016) analyzed the RMs from 1383 of extragalactic polarized sources and found values between -200 and +200 rad m⁻² were common at R_{500} . The corresponding magnetic field strengths they deduced were \sim a few microGauss (Böhringer et al. 2016). In Section 5 we

discuss how cluster FRBs from future surveys could better constrain magnetic fields in and around the ICM.

3.4. Mean Temperature from DM

The ICM observables that we discuss in this work are DM, RM, X-ray brightness, and the SZ-y parameter. Each is a weighted integral of n_e along the line of sight. In Faraday rotation, the gas density is weighted by magnetic field strength, $B_{//}$. For X-ray luminosity, emission is the sum of n_e^2 weighted by $\Lambda(T_e)$. In the case of the SZ-y parameter, n_e is weighted by T_e itself. X-ray derived density and SZ-derived pressure are commonly used to estimate temperature (Eckert et al. 2013). Alternatively, the ratio of X-ray luminosity to $y_{\rm SZ}$ has been taken to constrain the gas temperature. For example, Planck Collaboration et al. (2016c) find the ratio of X-ray luminosity to $y_{\rm SZ}$ for the Virgo cluster at angular position θ to be $\langle n_e \Lambda(T_e)/\langle k_B T_e \rangle \rangle(\theta)$. This quantity offers information on the cluster temperature profile under certain assumptions about $n_e(r)$ and Λ .

We can attempt something similar using the ratio of y_{SZ} to DM_{ICM}, which will be independent of n_e . Evaluating Equations (2) and (3) at impact parameter b_{\perp} we get

$$y_{\rm SZ}(b_{\perp}) \approx \frac{k_B T_e}{m_e c^2} \sigma_T \langle n_e \rangle L_{\rm ICM}$$
 (9)

$$\mathrm{DM}_{\mathrm{ICM}}(b_{\perp}) \approx \langle n_e \rangle \, L_{\mathrm{ICM}},$$
 (10)

where L_{ICM} is the line-of-sight length scale of the cluster at that b_{\perp} . By taking their ratio and rearranging, we can make a crude approximation for the mean plasma temperature at that physical offset,

$$\langle T_e(b_\perp) \rangle \approx \frac{m_e c^2}{\sigma_T k_B} \frac{y_{sz}}{DM_{ICM}}$$
 (11)

=1.15 × 10⁷ K
$$\left(\frac{y_{SZ}}{10^{-6}}\right) \left(\frac{DM}{250 \frac{pc}{cm^3}}\right)^{-1}$$
. (12)

We estimate the projected y_{sz} at each cluster's b_{\perp} from our fits to the Planck data described in Section 2. This gives $y_{\rm SZ} = (3.31 \pm 1.36) \times 10^{-6}$ for A2310 at 520 kpc and $y_{\rm SZ} = (6.80 \pm 3.03) \times 10^{-7}$ for A2311 at 870 kpc. Plugging these values into Equation (12), we find $\langle k_B T_e \rangle \approx 0.8$ –3.9 keV for A2310, in agreement with the expected electron temperature for a cluster of similar mass at that impact parameter (Vikhlinin et al. 2005; Pratt et al. 2007). This is the first time halo gas temperature has been measured using FRBs. For A2311 at 870 kpc we find $\langle k_B T_e \rangle \approx 0.6$ –16 keV along that line of sight. The large range in temperature is primarily due to the uncertainty in ICM DM for FRB 20220509G.

While it is hard to match the statistical precision of an X-ray spectroscopic temperature measurement, there are benefits to using FRB DMs to derive gas temperature: with FRBs we do not need to account for "clumping" effects due to the n_e^2 dependence (Eckert et al. 2015); the temperature will be approximately mass weighted rather than measured by the more complicated weighting intrinsic to spectroscopic measurements (Mazzotta et al. 2004), and current X-ray facilities are generally not sensitive beyond $\sim R_{500}$. The obvious drawbacks of using FRBs are that we have only a single sight line, and the DM contribution of the IGM, Milky Way, and the

host galaxy must be modeled. The former will be alleviated by FRB surveys with high areal density, providing multiple sight lines through individual halos. The latter may be aided by cross correlation (e.g., Madhavacheril et al. 2019; Raf 2021), which are less sensitive to host DM contamination. In Section 5 we describe how future surveys will allow for statistical FRB/cluster studies.

4. Comparison with Simulations

We use the IllustrisTNG simulation (Nelson et al. 2019) to estimate typical DM values of the ICM as a function of impact parameter. We seek also to estimate the variance between galaxy clusters of similar mass and variance within a cluster for different PAs at fixed impact parameter. The clusters were extracted from the TNG300-1 Snapshot number 98, corresponding to redshift 0.01.

We first extract cylinders of length 300 Mpc and radius 5 Mpc from the simulation box. These allow us to estimate not only the ICM contribution to DM but also the IGM along that sightline. We then calculate gas properties for each cell in that cylinder and estimate free electron density as

$$n_e = f_e \ \rho_o \ / m_p, \tag{13}$$

where f_e is the free electron abundance, ρ_g is gas density, and m_p is the proton mass. The *i*th cell's contribution to the total DM is

$$DM_{i} = n_{a}^{i} \Delta r_{i} (1 + z_{i})^{-1}, \tag{14}$$

where Δr_i is the distance through the cell at an impact parameter b_i . The cell's redshift is z_i . For cell size, Δx , $\Delta r_i = 2\sqrt{\Delta x^2 - b_i^2}$. The total DM is then ΣDM_i for all cells that are intersected by the FRB.

We compute DM profiles for all halos in TNG300-1 that have $M_{500} > 10^{13.5} \, M_{\odot}$. In Figure 6 we show four galaxy clusters with masses comparable to the masses of host clusters of FRB 20220509G and FRB 20220914A. The blue and green data points in the bottom row correspond to the estimated ICM contribution to the two FRB DMs, which agree well with the expected range at their respective impact parameters. There is significant variance within a cluster even at a fixed impact parameter, particularly beyond the virial radius (corresponding to $\approx 1500 \, \text{kpc}$ given $R_{500} \approx 800 \, \text{kpc}$ for these clusters). There is also some scatter between clusters, but the DM curves are roughly consistent. The mean values in DM versus b_{\perp} (solid purple lines in Figure 6) are also in agreement with analytic models for the cluster gas density (Vikhlinin et al. 2005; Prochaska & Zheng 2019).

Compared to simulations of the CGM or gas in galaxy groups, simulations of galaxy clusters are in relatively good agreement with one another as well as with observations (Oppenheimer et al. 2021). As the sophistication of cosmological MHD simulations progresses, they will be an invaluable tool for understanding the properties of FRBs that are impacted by cluster gas. This is especially true for magnetic field inference from FRB RMs and for gas temperatures outside of R_{500} as outlined in the following section.

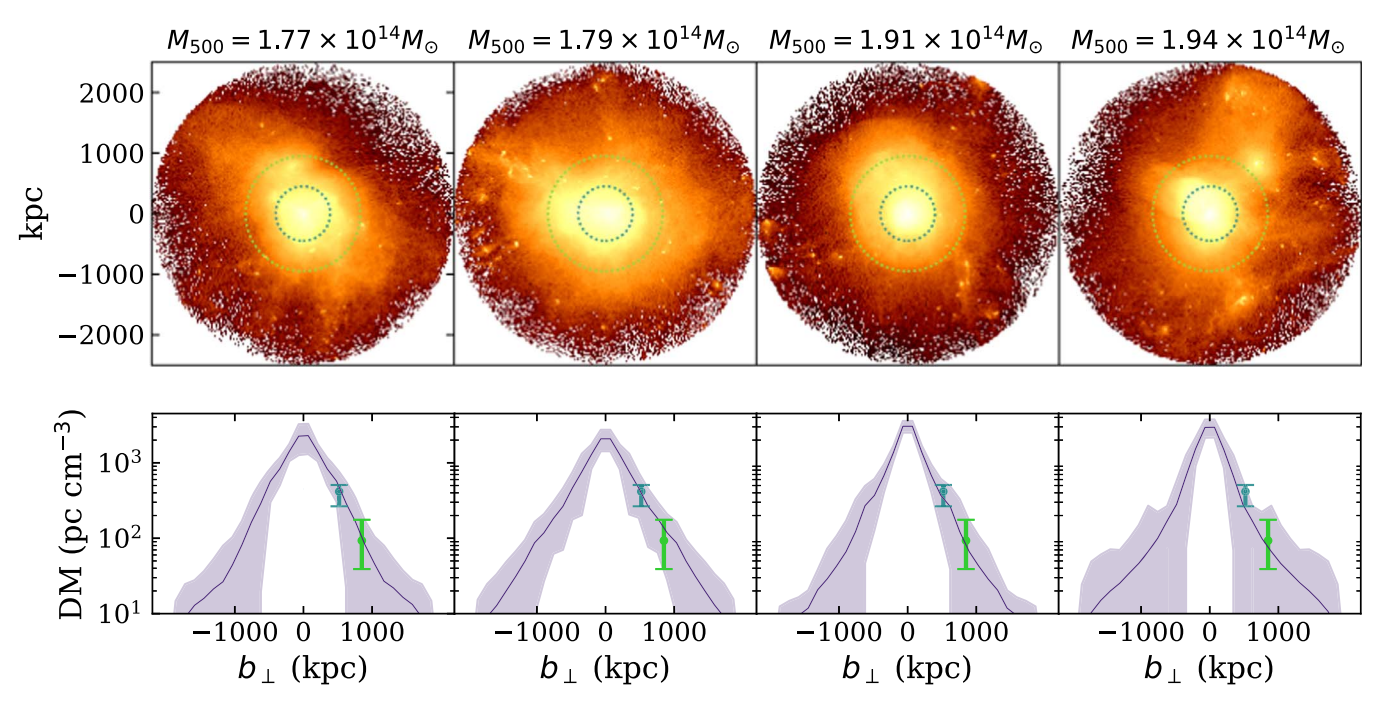


Figure 6. Four galaxy clusters from the TNG300-1 simulation whose masses are similar to those of A2310 and A2311. The top row shows gas surface density within 2 Mpc of the cluster center. The green and blue circles represent the impact parameter of FRB 20220509G and FRB 20220914A, respectively. The bottom row shows DM_{ICM} as a function of impact parameter, b_{\perp} , with error bars for the two observed cluster FRBs. The solid purple line is the median DM over fifty azimuthal angles, and the shaded region shows the 90% limits at that b_{\perp} . The curves assume the FRB is embedded halfway in the ICM, i.e., $l_{\text{LOS}} = 0$.

5. Discussion

5.1. Beyond the Virial Radius

Outside of the virial radii of galaxy clusters, plasma is difficult to observe via X-ray. FRB DMs, however, are more sensitive to this gas due to the n_e (rather than n_e^2) dependence and can constrain to ICM and WHIM on the outskirts of clusters. Fujita et al. (2017) have shown that by combining FRB DMs with the pressure profiles from SZ observations, the temperature profile of the WHIM can be obtained beyond $1.5\,R_{200}$.

In future FRB surveys, large numbers of localized FRBs will produce DM maps with high areal density, intersecting individual clusters along multiple sight lines. For example, the proposed DSA-2000 survey will spend roughly 5% of its time on deep-drilling fields that overlap with Rubin, XMM-LSS, Extended Chandra Deep Field-South, and COSMOS deep fields (Hallinan et al. 2019b). This will lead to roughly 500 FRBs in just $\sim \! 10 \, \text{deg}^2$. Nearly every massive galaxy cluster out to z = 0.3 will be intersected by at least one FRB sight line. We will have a wealth of multiwavelength data in this field, including SZ data and deep X-ray observations. Such a data set will allow us to constrain the magnetic field in the ICM and the density profile in the WHIM, as well as gas temperatures outside of R_{500} . However, from Figure 6 we see substantial azimuthal and intercluster variance in DM at large radii. Analyses of the gas beyond R_{500} ought to be done in tandem with cosmological MHD simulations.

5.2. Prevalence of Cluster FRBs

Roughly 5% of sight lines from FRBs at $z \approx 0.5$ are expected to intersect galaxy clusters in the foreground (Prochaska & Zheng 2019). However, if an FRB sight line has a projected offset from a cluster that is less than R_{200} , it is more likely that

the FRB came from the cluster itself than from behind it, assuming the rate of FRBs is related to stellar mass and not just star formation. This is because the overdensity of galaxies within massive halos is enough to counter the larger volume behind the galaxy cluster. Using $R_{200} \approx 1$ Mpc, the comoving volume in the region of a cone behind a redshift 0.25 cluster out to z=0.5 is $\sim 7 \times 10^3$ Mpc³. Assuming a galaxy number density of roughly 10^{-2} Mpc⁻³ (White et al. 2011), the volume behind the cluster should have only $\mathcal{O}(70)$ galaxies, compared with 10^{2-3} galaxies in the cluster. We note again that this rough estimate assumes cluster galaxies are as likely as noncluster galaxies to produce FRBs. We have also ignored luminosity function considerations, which make FRBs behind the cluster to be more difficult to detect because they are less bright. It is therefore unsurprising that the first two localized FRBs that are known to be impacted by the ICM have come from member galaxies of clusters and not from behind clusters.

We have crossmatched twelve sources localized by the DSA-110 with cluster catalogs and found two FRBs that reside in galaxy clusters. This suggests the fraction of FRBs from galaxy clusters is $f_{\rm cFRB}=0.17^{+0.36}_{-0.12}$, using a 90% Poissonian confidence interval. We do not include other localized FRBs because we are not aware of concerted efforts to crossmatch those FRB positions with clusters.

The large value of $f_{\rm cFRB}$ has interesting implications for FRBs detected at other surveys and on our interpretation of observables such as the FRB DM distribution. CHIME/FRB detects $\mathcal{O}(10^3)$ FRBs per year, without sufficient localization precision to identify a host galaxy. They may therefore already have detected hundreds of sources that reside in galaxy clusters. The host ICM could then dominate the high-DM tail of the total observed DM distribution (James et al. 2022), which would otherwise be interpreted as the most distant sources. Even with arcminute localizations, a careful statistical

crossmatch of CHIME/FRB sources with galaxy cluster catalogs could reveal this signal.

5.3. FRB Progenitor Implications

FRB 20220509G is the first source to belong to an early-type galaxy. This fits an emerging picture that FRBs can be produced in a variety of environments, including dense starforming regions, globular clusters, and pristine environments with little H II (Tendulkar et al. 2017; Marcote et al. 2020; Pastor-Marazuela et al. 2021; Kirsten et al. 2022; Niu et al. 2022). The full implications of FRB 20220509G's quiescent host will be fleshed out by Sharma et al. (2023). If more FRBs are localized to cluster galaxies with low rates of star formation, then progenitor models must explain evolutionary channels that can produce FRBs in the absence of recent corecollapse supernovae. This would be promising for FRB applications research as early-type galaxies are not expected to have significant magnetoionic plasma in their ISM or H II regions near the source, alleviating the problem of disentangling host DM, RM, and scattering from cosmological contributions.

6. Conclusion

We have discovered two FRB sources that reside in massive galaxy clusters. The host galaxy of FRB 20220914A is a member of cluster A2310, whose ICM dominates the DM budget of the FRB. We have combined the DM of FRB 20220914A with SZ observations of A2310 to make the first estimate of the mean line-of-sight temperature of gas using an FRB. FRB 20220509G belongs to an early-type galaxy (Sharma et al. 2023) at a projected offset of 870 kpc from the center of cluster A2311. That cluster's ICM is found to contribute 16-172 pc cm⁻³ to the FRB DM, which is consistent with analytic models and simulations of the ICM for a cluster with mass $M_{500} \approx 1.5 - 2 \times 10^{14} M_{\odot}$. Polarization analysis of the burst found significant Faraday rotation. Assuming this RM originates in the ICM, we constrain the mean line-of-sight magnetic field strength to be $0.75-7 \mu G$ in the intracluster gas. Roughly 17% of our first sample of localized FRBs were found to reside in galaxy clusters. While we expect this fraction to come down with time, galaxy clusters will likely play a significant role in upcoming FRB surveys, particularly in attempts at mapping out the universe's baryons.

The authors thank staff members of the Owens Valley Radio Observatory and the Caltech radio group, including Kristen Bernasconi, Stephanie Cha-Ramos, Sarah Harnach, Tom Klinefelter, Lori McGraw, Corey Posner, Andres Rizo, Michael Virgin, Scott White, and Thomas Zentmyer. Their tireless efforts were instrumental to the success of the DSA-110. The DSA-110 is supported by the National Science Foundation Mid-Scale Innovations Program in Astronomical Sciences (MSIP) under grant AST-1836018. We acknowledge use of the VLA calibrator manual and the radio fundamental catalog. Some of the data presented herein were obtained at the W. M. Keck Observatory, which is operated as a scientific partnership among the California Institute of Technology, the University of California and the National Aeronautics and Space Administration. The Observatory was made possible by the generous financial support of the W. M. Keck Foundation. We thank Ryuichi Takahashi and Weiwei Xu for helpful

discussions and materials related to their overlapping work. We also thank Nicholas Battaglia for useful discussion.

Facilities: Keck:I (LRIS), Keck:II (ESI).

Software: astropy, CASA, frb, heimdall, lpipe, pPXF, Prospector, wsclean.

ORCID iDs

Liam Connor https://orcid.org/0000-0002-7587-6352
Vikram Ravi https://orcid.org/0000-0002-7252-5485
Ge Chen https://orcid.org/0000-0003-2867-4544
Jakob T. Faber https://orcid.org/0000-0001-9855-5781
James W. Lamb https://orcid.org/0000-0002-5959-1285
Gregg Hallinan https://orcid.org/0000-0002-7083-4049
Casey Law https://orcid.org/0000-0002-4119-9963
Jack Sayers https://orcid.org/0000-0002-8213-3784
Kritti Sharma https://orcid.org/0000-0002-4477-3625
Myles B. Sherman https://orcid.org/0000-0002-6573-7316
Jun Shi https://orcid.org/0000-0003-1647-7762
Dana Simard https://orcid.org/0000-0002-8873-8784
Jean Somalwar https://orcid.org/0000-0001-8426-5732
Reynier Squillace https://orcid.org/0000-0001-6748-5290
Nitika Yadlapalli https://orcid.org/0000-0003-3255-4617

References

```
Abell, G. O. 1958, ApJS, 3, 211
Agarwal, D., Lorimer, D. R., Fialkov, A., et al. 2019, MNRAS, 490, 1
Anna-Thomas, R., Connor, L., Burke-Spolaor, S., et al. 2023, Sci, 380, 599
Arnaud, M., Pratt, G. W., Piffaretti, R., et al. 2010, A&A, 517, A92
Beniamini, P., Kumar, P., & Narayan, R. 2022, MNRAS, 510, 4654
Bhandari, S., Sadler, E. M., Prochaska, J. X., et al. 2020, ApJL, 895, L37
Bhardwaj, M., Gaensler, B. M., Kaspi, V. M., et al. 2021, ApJL, 910, L18
Böhringer, H., Chon, G., & Kronberg, P. P. 2016, A&A, 596, A22
Böhringer, H., & Werner, N. 2010, A&ARv, 18, 127
Budzynski, J. M., Koposov, S. E., McCarthy, I. G., McGee, S. L., &
   Belokurov, V. 2012, MNRAS, 423, 104
Carilli, C. L., & Taylor, G. B. 2002, ARA&A, 40, 319
Chambers, K. C., Magnier, E. A., Metcalfe, N., et al. 2016, arXiv:1612.05560
Chatterjee, S., Law, C. J., Wharton, R. S., et al. 2017, Natur, 541, 58
Connor, L., & Ravi, V. 2022, NatAs, 6, 1035
Connor, L., Sievers, J., & Pen, U.-L. 2016, MNRAS, 458, L19
Cook, A. M., Bhardwaj, M., Gaensler, B. M., et al. 2023, ApJ, 946, 58
Cordes, J. M., & Chatterjee, S. 2019, ARA&A, 57, 417
Cordes, J. M., & Lazio, T. J. W. 2002, arXiv:astro-ph/0207156
CHIME/FRB Collaboration, Amiri, M., Andersen, B. C., et al. 2021, ApJS,
   257, 59
CHIME/FRB Collaboration, Andersen, B. C., Bandura, K., et al. 2019, ApJL,
  885, L24
Dey, A., Schlegel, D. J., Lang, D., et al. 2019, AJ, 157, 168
Eckert, D., Ghirardini, V., Ettori, S., et al. 2019, A&A, 621, A40
Eckert, D., Molendi, S., Vazza, F., Ettori, S., & Paltani, S. 2013, A&A,
Eckert, D., Roncarelli, M., Ettori, S., et al. 2015, MNRAS, 447, 2198
Fujita, Y., Akahori, T., Umetsu, K., Sarazin, C. L., & Wong, K.-W. 2017, ApJ,
Ghirardini, V., Eckert, D., Ettori, S., et al. 2019, A&A, 621, A41
Hallinan, G., Dong, D., & Ravi, V. 2019a, ATel, 13018, 1
Hallinan, G., Ravi, V., Weinreb, S., et al. 2019b, BAAS, 51, 255
Heintz, K. E., Prochaska, J. X., Simha, S., et al. 2020, ApJ, 903, 152
Hutschenreuter, S., Anderson, C. S., Betti, S., et al. 2022, A&A, 657, A43
Hitomi Collaboration, Aharonian, F., Akamatsu, H., et al. 2016, Natur,
  535, 117
James, C. W., Prochaska, J. X., Macquart, J. P., et al. 2022, MNRAS,
   509, 4775
Kirsten, F., Marcote, B., Nimmo, K., et al. 2022, Natur, 602, 585
Lee, K.-G., Ata, M., Khrykin, I. S., et al. 2022, ApJ, 928, 9
Lees, J. F. 1992, PASP, 104, 154
Macquart, J. P., Prochaska, J. X., McQuinn, M., et al. 2020, Natur, 581, 391
Madhavacheril, M. S., Battaglia, N., Smith, K. M., & Sievers, J. L. 2019,
   PhRvD, 100, 103532
```

```
Marcote, B., Nimmo, K., Hessels, J. W. T., et al. 2020, Natur, 577, 190
Marinacci, F., Vogelsberger, M., Pakmor, R., et al. 2018, MNRAS, 480, 5113
Masui, K., Lin, H.-H., Sievers, J., et al. 2015, Natur, 528, 523
Mazzotta, P., Rasia, E., Moscardini, L., & Tormen, G. 2004, MNRAS, 354, 10
McQuinn, M. 2016, ARA&A, 54, 313
Mroczkowski, T., Nagai, D., Basu, K., et al. 2019, SSRv, 215, 17
Nelson, D., Springel, V., Pillepich, A., et al. 2019, ComAC, 6, 2
Niu, C. H., Aggarwal, K., Li, D., et al. 2022, Natur, 606, 873
Ocker, S. K., Cordes, J. M., Chatterjee, S., et al. 2023, MNRAS, 519, 821
Ocker, S. K., Cordes, J. M., Chatterjee, S., & Gorsuch, M. R. 2022, ApJ,
Oppenheimer, B. D., Babul, A., Bahé, Y., Butsky, I. S., & McCarthy, I. G.
   2021, Univ, 7, 209
Pastor-Marazuela, I., Connor, L., van Leeuwen, J., et al. 2021, Natur, 596, 505
Petroff, E., Barr, E. D., Jameson, A., et al. 2016, PASA, 33, e045
Petroff, E., Hessels, J. W. T., & Lorimer, D. R. 2019, A&ARv, 27, 4
Piffaretti, R., Arnaud, M., Pratt, G. W., Pointecouteau, E., & Melin, J. B. 2011,
       4, 534, A109
Pratt, G. W., Böhringer, H., Croston, J. H., et al. 2007, A&A, 461, 71
Pratt, G. W., Croston, J. H., Arnaud, M., & Böhringer, H. 2009, A&A,
Prochaska, J. X., & Zheng, Y. 2019, MNRAS, 485, 648
Planck Collaboration, Ade, P. A. R., Aghanim, N., et al. 2014, A&A, 571, A20
Planck Collaboration, Ade, P. A. R., Aghanim, N., et al. 2016a, A&A,
  594, A27
```

```
Planck Collaboration, Aghanim, N., Arnaud, M., et al. 2016b, A&A, 594, A22
Planck Collaboration, Ade, P. A. R., Aghanim, N., et al. 2016c, A&A,
  596, A101
Ravi, V. 2019, ApJ, 872, 88
Ravi, V., Catha, M., Chen, G., et al. 2023a, ApJL, 949, L3
Ravi, V., Catha, M., Chen, G., et al. 2023b, arXiv:2301.01000
Ravi, V., Catha, M., D'Addario, L., et al. 2019, Natur, 572, 352
Raf 2021, ApJ, 922, 42
Sarazin, C. L. 1986, RvMP, 58, 1
Sayers, J., Golwala, S. R., Mantz, A. B., et al. 2016, ApJ, 832, 26
Seta, A., Rodrigues, L. F. S., Federrath, C., & Hales, C. A. 2021, ApJ, 907, 2
Sharma, K., Somalwar, J., Law, C., et al. 2023, arXiv:2302.14782
Simard, D., & Ravi, V. 2021, arXiv:2107.11334
Tendulkar, S. P., Bassa, C. G., Cordes, J. M., et al. 2017, ApJL, 834, L7
Tumlinson, J., Peeples, M. S., & Werk, J. K. 2017, ARA&A, 55, 389
van Weeren, R. J., de Gasperin, F., Akamatsu, H., et al. 2019, SSRv, 215, 16
Vikhlinin, A., Markevitch, M., Murray, S. S., et al. 2005, ApJ, 628, 655
Voit, G. M. 2005, RvMP, 77, 207
White, D. J., Daw, E. J., & Dhillon, V. S. 2011, CQGra, 28, 085016
Xu, W., Ramos-Ceja, M. E., Pacaud, F., Reiprich, T. H., & Erben, T. 2022,
   A&A, 658, A59
Yang, X., Xu, H., He, M., et al. 2021, ApJ, 909, 143
Yao, J. M., Manchester, R. N., & Wang, N. 2017, ApJ, 835, 29
Zhang, Z. J., Yan, K., Li, C. M., Zhang, G. Q., & Wang, F. Y. 2021, ApJ,
```